



Research Article

Investigation of the electrochemical intercalation of Ca^{2+} into graphite layer carbon nano filaments as a novel electrode material for calcium-ion batteries

Yuichiro Nishimura¹ · Shuzo Yamazaki¹ · Takahiro Sakoda³ · Kiyoharu Nakagawa^{1,2} 

Received: 9 August 2022 / Accepted: 3 January 2023

Published online: 18 January 2023

© The Author(s) 2023 **OPEN**

Abstract

We investigated the electrochemical intercalation of Ca^{2+} or solvated Ca^{2+} into Marimo nano carbon (MNC) as an anode material for calcium-ion batteries. When $\text{Ca}(\text{ClO}_4)_2$ and $\text{Ca}(\text{TFSI})_2$ were used as electrolyte salts, the solution structure changed in the γ -butyrolactone solvent. Additionally, higher charge capacitance was obtained at the MNC electrode than at the graphite electrode. When heat-treated MNCs were used with each electrolyte (ClO_4)₂ intercalated better than $\text{Ca}(\text{TFSI})_2$.

Article Highlights

- Marimo nano carbon, an aggregate of carbon nanofilaments, was shown to intercalate Ca^{2+} or solvated Ca^{2+} .
- The graphite structure of carbon nanofilaments was developed via heat treatment.
- The strength of interaction with solvent molecules differed depending on the Ca salt.
- Marimo nano carbon exhibited higher charge/discharge capacity than natural graphite.

Keywords Calcium-ion battery · Carbon nanofilament · Electrochemical intercalation · Heat treatment · Marimo nano carbon

1 Introduction

Lithium-ion batteries (LIBs) are used in various electronic devices such as mobile phones and electric vehicles owing to their high energy density, high voltage, and long life. Because of technological innovations in these electrical devices, the demand for LIBs has been growing rapidly around the world. However, because the energy density of commercially available LIBs is already approaching the theoretical value, the development of new power storage devices that can replace LIBs crucial [1]. Therefore,

secondary batteries utilizing multivalent cations (Mg^{2+} and Ca^{2+}) instead of Li^+ have been attracting attention with regard to the development of post LIBs [2–7]. Among these multivalent cation batteries, calcium-ion batteries (CIBs) utilizing Ca^{2+} as charge carriers have great potential as alternatives to LIBs [8–10]. Because CIBs use multivalent cations, they can achieve twice the capacity of LIBs. Additionally, because the standard electrode potential of Ca^{2+} is approximately 0.5 V lower than that of Mg^{2+} (–2.87 and –2.37 V with respect to the Standard hydrogen electrodes of Ca and Mg, respectively), CIBs can achieve

✉ Kiyoharu Nakagawa, kiyoharu@kansai-u.ac.jp | ¹Department of Chemical, Energy and Environmental Engineering, Kansai University, 3-3-35, Yamatecho, Suita, Osaka 564-8680, Japan. ²High Technology Research Core (HRC), Kansai University, 3-3-35, Yamatecho, Suita, Osaka 564-8680, Japan. ³Toyo Tanso Co., Ltd., 2791 Matsusaki, Takumacho, Mitoyo, Kagawa 769-1102, Japan.



high operating voltages [1]. Moreover, because Ca^{2+} is the fifth most abundant element in the Earth's crust, it is advantageous in terms of sustainability [11]. Therefore, CIBs have more attractive features when compared with LIBs and other multivalent ion batteries. However, some problems exist concerning the development of CIBs for practical use. [12, 13]. Particularly, the use of Ca^{2+} metal anodes is not appropriate because the surface film formed on the Ca^{2+} metal prevents the reversible plating/stripping overpotentials of Ca^{2+} in conventional organic electrolytes. [12–14]. Furthermore, because multivalent cations, such as Ca^{2+} , exhibit stronger Lewis acidity than Li^+ , they form strong solvation structures with the solvent molecules in electrolytes. Thus, high desolvation energy is required for intercalation into the host material, affording poor kinetics of charge intercalation [12, 15]. Therefore, optimization of Ca^{2+} host materials is desired to address these limitations.

To eliminate the instability of plating/stripping overpotentials of the Ca^{2+} metal electrode, a type of CIBs utilizing the Ca^{2+} intercalation/deintercalation reaction into the host material was proposed [16–20]. Graphite is one of the candidates as an anode material of CIBs because it can accommodate various guest ions into its layers and form a graphite intercalation compound (GIC). Graphite is generally used as an anode material for commercialized LIBs because of its inexpensiveness, safety, and capacity. In LIBs, Li^+ is stored in the graphite layers to form a Li–GIC [21]. The intercalation of Ca^{2+} into graphite layers was previously limited to reports based on chemical methods only [22–24]. Recently, however, some reports suggested that the electrochemical intercalation of Ca^{2+} into graphite was possible [25]. These reports indicated that the potential carbonaceous materials could be used as anode materials for CIBs, and a charge/discharge system like that in LIBs could be constructed.

Therefore, instead of graphite, Marimo nano carbon (MNC) was investigated as a new anode material for CIBs. MNC is a spherical carbon material that comprises high-density carbon nanofilaments (CNFs) or carbon nanotubes arranged radially [26]. Furthermore, synthesized CNFs have remarkable properties: their internal structure (such as cup-stacked, coin-stacked, and hollow) can be controlled by the type of the catalyst metal [27]. Additionally, in cup-stacked and coin-stacked CNFs, the edge planes of the graphene sheets are exposed. Thus, they might be applied in a wide range of fields. As reported previously the use of coin-stacked CNFs with a graphite structure as an anode material for LIBs yielded higher capacity than that of a graphite anode [28]. Thus, the MNC anode may intercalate more Ca^{2+} between the graphene layers of CNF than the graphite anode. Consequently, higher charge/discharge capacities than graphite may be obtained. In this study, MNC with coin-stacked CNFs was synthesized as the anode

material for CIBs. Additionally, heat-treated MNC (Ht-MNC) was prepared to increase the crystallinity of CNFs, and the performances of MNC and Ht-MNC as anode materials for CIBs were evaluated.

2 Experimental

Oxidized diamond (Diamond Innovations Co., Ltd.) was used as a catalyst support. It has oxygen-containing functional groups arranged regularly, therefore nano metal particles can be highly dispersed on it [29]. Therefore, an oxidized-diamond-supported Pd catalyst (Pd loading: 5 wt%) was prepared for CNF synthesis using the metal nanocolloidal method [30]. Oxidized diamond was added to deionized water, and the resultant dispersion was stirred for 30 min under ultrasonic treatment. PdCl_2 as a precursor and citric acid as a dispersing agent were added, and the resultant solution was stirred for 30 min under ultrasonic treatment. Moreover, NaBH_4 as a reducing agent was added to the solution. After stirring for 30 min under ultrasonic treatment, the supernatant was removed from the solution via centrifugation and dried at 60 °C. The supported catalysts were calcined at 450 °C for 5 h in N_2 prior to the reaction.

MNC was synthesized via chemical vapor deposition (CVD) method using a horizontal rotating fluidized bed reactor [31]. We took 200 mg of the oxidized-diamond-supported Pd catalyst and uniformly distributed it on a quartz boat. After inserting the quartz boat into the center of the quartz tube, the reactor temperature was elevated to 600 °C under a N_2 atmosphere. Subsequently, C_2H_4 was introduced at 30 mL min^{-1} and 600 °C. The reaction time was 1 h. The heat treatments of MNC were conducted at 2500 °C for 1 h under vacuum.

Field emission scanning electron microscopy (FE-SEM; S-4800, Hitachi, Ltd.) was conducted to observe the surface structure of MNC, and transmission electron microscopy (TEM; JEM-2010K, JEOL Ltd.) was conducted to observe the internal structure of the synthesized CNFs. Moreover, X-ray diffractometry (XRD; SmartLab, Rigaku) was conducted to calculate the interlayer distance before and after discharging from the peak position corresponding to the (002) plane of the graphite structure as follows:

$$d = \frac{\lambda}{2\sin\theta_c}, \quad (1)$$

where d denotes the phase-spacing, λ is the (Cu-K α) X-ray wavelength, and θ_c is the diffraction angle of graphite. The X-ray wavelength was 0.15406 nm, the voltage was 45 kV, and the current was 200 mA. The divergence slit width was 1/2°, receiving slit width was 0.15 mm, and scattering

slit width was $1/2^\circ$. The range of the measurement was 5° – 90° , and the scan speed was $50^\circ \text{ min}^{-1}$. The measurement was conducted after three cycles of discharging and charging to obtain representative results. Laser Raman spectroscopy (NRS-3100, JASCO) was conducted to analyze the degree of graphitization of the synthesized CNFs and the solvation structure. The excitation wavelength of the laser light source was 532 nm, and the laser power was 100 mW. The measurement was conducted with an exposure time of 5 s and comprised eight integrations. The wavenumber of the Raman shift was calibrated using Si and polypropylene standards. The surface area of the MNC was evaluated via the Brunauer–Emmett–Teller (BET) analysis of N_2 adsorption isotherms at 77 K, and it was measured using a specific surface area analyzer (BELSORP-mini, Nippon Bel, Japan). Fourier transform infrared spectroscopy (FTIR; FT/IR-4200, JASCO) was conducted to analyze the solution structure. The measurement range was 500 – 4000 cm^{-1} at a resolution of 4 cm^{-1} and the integration number was 400. The solution structure was evaluated using the liquid-film method using a CaF_2 window board.

MNC and Ht-MNC were used as working electrode materials, and spherical natural graphite (CGB-10; Nippon Graphite Industries, Ltd.) was used as a reference material. The MNC and graphite electrodes were mixtures of 95 wt% respective active materials and 5 wt% polyvinylidene fluoride (Sigma-Aldrich). Subsequently *N*-methylpyrrolidone was added to the mixtures to make a slurry. The slurry was coated onto Cu foil using the doctor blade method. After drying, the resulting electrode was punched to a diameter of 12 mm. Activated carbon (AC; YP-50F, Kuraray, Co., Ltd.) was used as the counter/reference electrode material instead of the Ca metal [25]. The AC electrodes comprised 80 wt% of YP-50F as the active material, 10 wt% of carbon black (TOKABLACK; TOKAI CARBON Co., Ltd.) as the conductivity promoter, and 10 wt% of Teflon resin as the binder. The mixture was rolled to a thickness of 0.1 mm and punched to a diameter of 12 mm. The MNC, Ht-MNC, graphite and AC electrodes were vacuum-dried at 80°C overnight before being used. Cellulose fiber (TF4050) was used as the separator. An electrolytic solution was prepared by dissolving 0.5 M $\text{Ca}(\text{ClO}_4)_2$ and 0.5 M $\text{Ca}(\text{TFSI})_2$ in γ -butyrolactone (GBL). These salts were dehydrated via lyophilization overnight. These chemicals were purchased from FUJIFILM Wako Pure Chemical Ltd. In this GBL-based electrolyte, a reversible redox reaction has been reported, and Raman spectroscopy has revealed that the reaction is due to Ca^{2+} intercalation/de-intercalation into the graphite layer. Therefore, GBL-based electrolytes were also used in this study [32].

Reference-electrode validation tests were performed via cyclic voltammetry (CV) measurements of

a three-electrode cell. A Pt electrode ($1 \text{ cm} \times 1 \text{ cm}$) was used as the working electrode, and the AC electrodes were employed as the counter and reference electrodes. Ferrocene (Fc) was added to the electrolyte at a concentration of 0.05 M, and 300 μL of electrolytic solution was added to each cell. The CV measurements were conducted in a scanning potential range from -0.6 to -1.0 V at a scan rate of 1 mV s^{-1} . To analyze the electrochemical behaviors of the MNC and Ht-MNC electrodes in organic electrolytes, charge/discharge measurements were conducted using an airtight flat cell (Fig. 1). The MNC, Ht-MNC, and graphite electrodes were used as the working electrodes, and the AC electrodes were employed as the counter electrodes. The charge/discharge measurements were conducted in a scanning potential range from -2.4 to 0 V and constant current of 0.1 C. All the cells were assembled in a N_2 -filled glove box, and all the electrochemical measurements were recorded using an electrochemical workstation (HZ-7000; Hokuto Denko, Japan).

3 Results and discussion

Figure 2 shows the SEM images of MNC and Ht-MNC. CNFs are densely generated and many pores exist between the fibers (Fig. 1a, a'). Moreover many CNFs of Ht-MNC thicker than the CNFs of MNC are observed. (Fig. 1b, b') The mean filament diameters of CNFs in the MNC and Ht-MNC were 24.1 and 70.8 nm, respectively.

Figure 3 shows the TEM images of CNFs of the MNC and Ht-MNC. As can be clearly seen from Fig. 3a, the synthesized CNFs have a coin-stacked structure, in which graphene sheets are stacked perpendicularly to the axis of the filaments. In Ht-MNC, the graphene sheets were stacked more regularly, and loops on the edge plane could be confirmed.

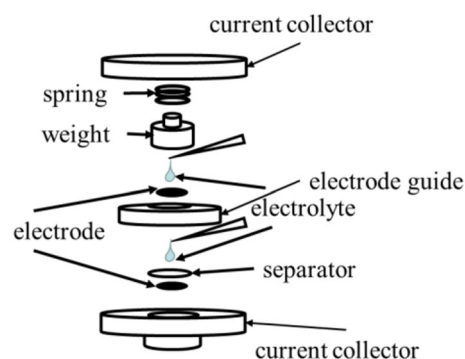


Fig. 1 Flat cell used during electrochemical measurement

Fig. 2 Field emission scanning electron microscopy images of **a** and **a'** Marimo nano carbon (MNC), **b** and **b'** heat-treated MNC (Ht-MNC)

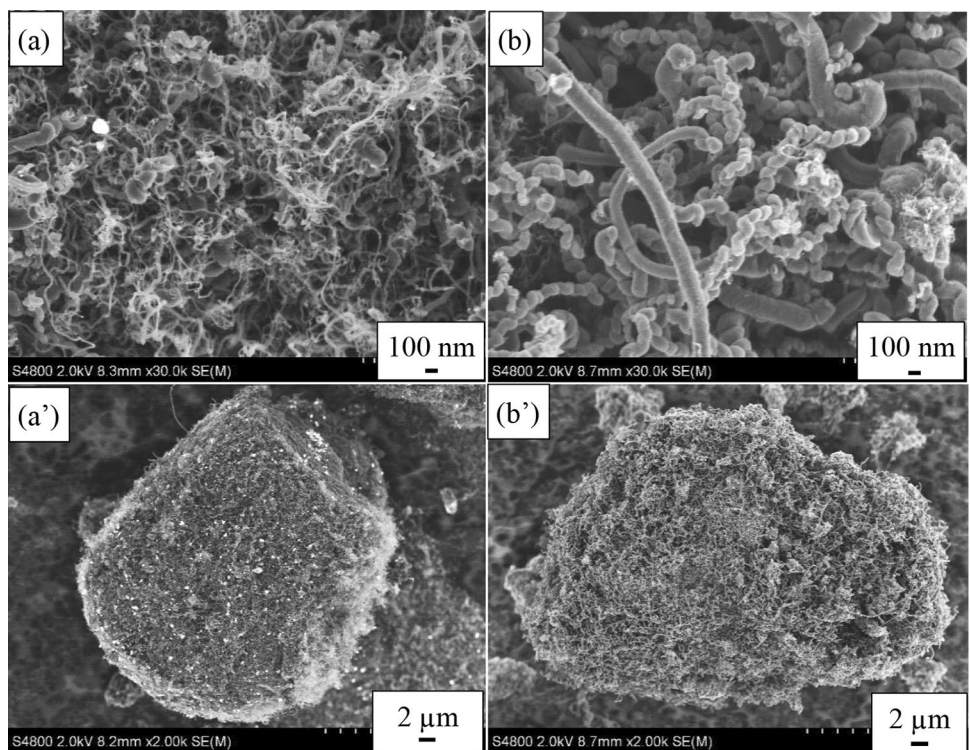


Fig. 3 Transmission electron microscopy (TEM) image of **a** synthesized and **b** heat-treated carbon nanofilaments (CNFs)

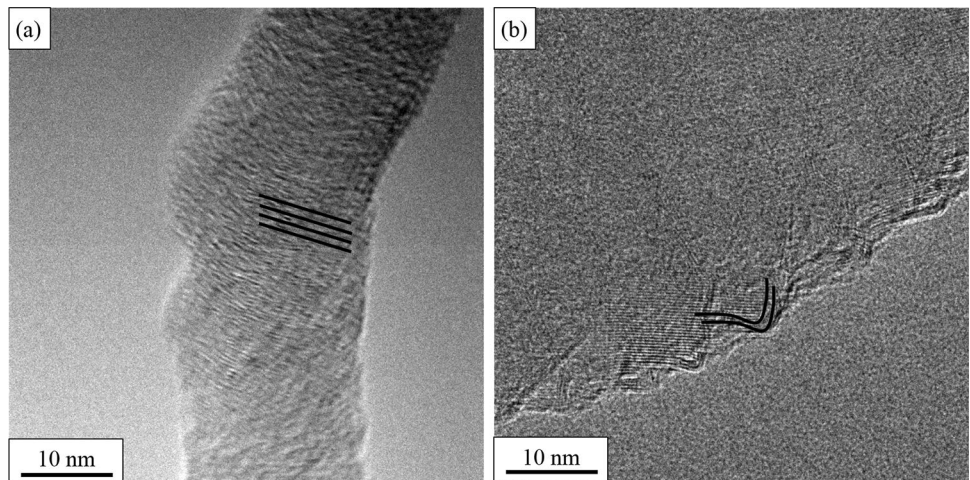


Fig. 4 Model of Marimo nano carbon (MNC)

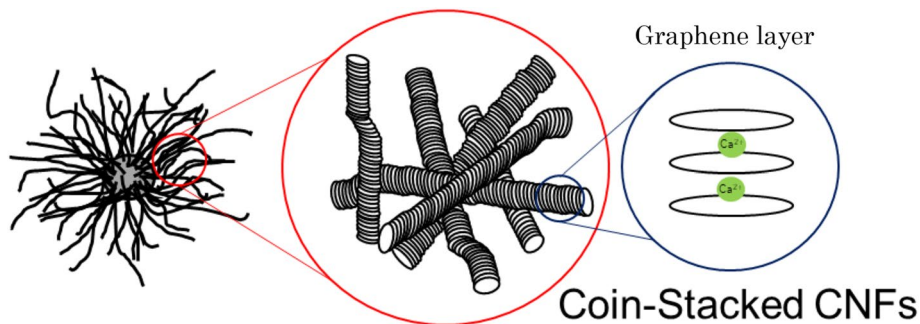


Figure 4 shows the model of MNC. MNC is a spherical carbon material that comprises (CNFs) or carbon nanotubes arranged radially. The CNFs synthesized in this study have a coin stacked structure.

XRD was conducted to evaluate the structures of MNC, Ht-MNC, and CGB-10 (see Fig. 5). Compared with MNC, the peak intensity of the (002) plane of graphite considerably increased for Ht-MNC, and the FWHM of the peak decreased from 3.01° to 0.98° accordingly (see Fig. 5a). Additionally, the peak position of the (002) plane also shifted from $2\theta = 25.81^\circ$ for MNC to $2\theta = 26.30^\circ$ for Ht-MNC, and the interlayer distances were 0.345 nm and 0.339 nm, respectively, as calculated from Eq. (1). Because the CVD method synthesizes CNFs at reasonably low temperatures, the CNFs in MNC had low crystallinity. However, a graphite structure is formed when a carbon material is heat-treated at $\geq 2000^\circ\text{C}$. Therefore, we hypothesize that the crystallinity of Ht-MNC was improved by reducing the defects of the carbon hexagonal network and developing the graphite structure via heat treatment. Additionally, the peaks derived from the Pd catalyst metal and oxidized diamond of the catalyst supports were confirmed for MNC, however, these peaks were not observed for Ht-MNC. Because the surface layer of diamond begins to graphitize at 1400°C and diamond completely transforms to graphite at 1900°C [33], the oxidized diamond transformed to a graphite structure via heat treatment at 2500°C . The carbon source was absorbed by CNFs owing to the graphitization of the

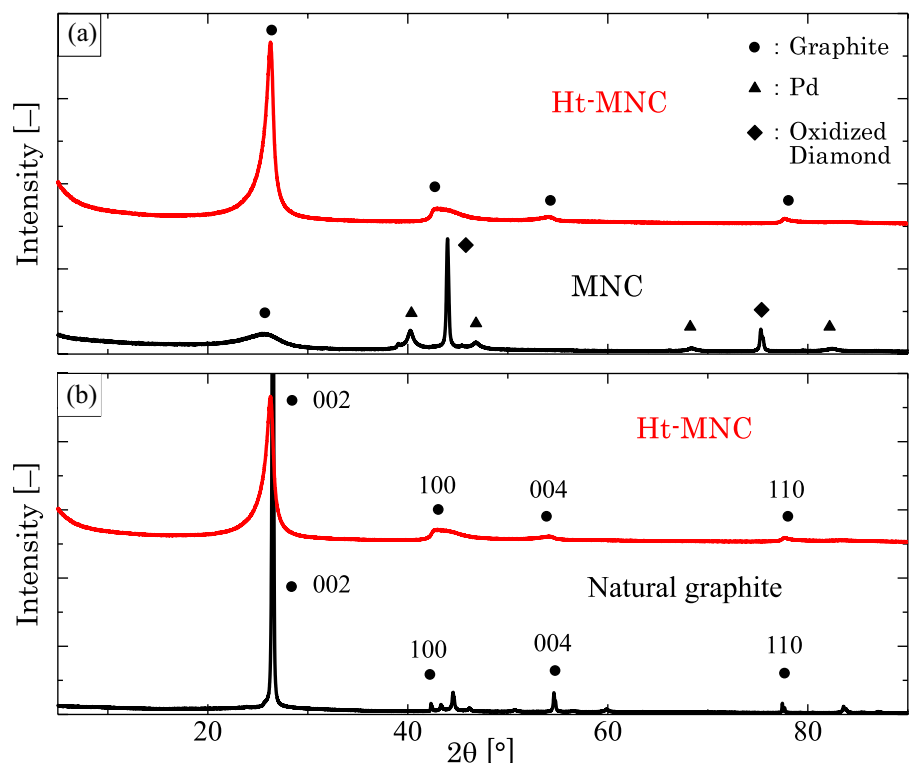
oxidized diamonds, thereby increasing the average fiber diameter. Figure 5b) compares Ht-MNC and natural graphite. For natural graphite, peaks derived from the (002), (100), (004), and (110) planes of graphite were confirmed. Similar peaks were confirmed for Ht-MNC, indicating the development of a graphite structure [34]. Because the synthesized CNFs have a coin-stacked internal structure (Fig. 3) with reported intercalation, the MNC anode may be able to intercalate Ca^{2+} or solvated Ca^{2+} between the graphene layers of the CNFs (Fig. 4).

Table 1 presents the physical properties of each sample, as derived via Raman, XRD and BET analysis. From the Raman spectrum, the crystallinity was evaluated from the peak intensity ratio (I_G/I_D) of the G-band (1580 cm^{-1}) due to the graphite structure and the D-band (1350 cm^{-1}) due to the defect. For MNC, the D-band appeared strong, whereas for Ht-MNC, the peak intensity of the D-band decreased and the I_G/I_D value increased. However, the I_G/I_D value for Ht-MNC was not as large as that of natural graphite. Therefore, a correlation was observed between the evaluation

Table 1 Characterization of each sample

Sample	I_G/I_D (-)	d002 (nm)	SBET(m^2/g)	V_{meso} (cm^3/g)
MNC	1.14	0.345	188.3	0.287
Ht-MNC	2.28	0.339	33.6	0.104
Natural graphite	3.36	0.336	7.1	0.019

Fig. 5 X-ray diffractometry (XRD) spectrum comparisons of **a** Marimo nano carbon (MNC) and heat-treated MNC (Ht-MNC), and **b** Ht-MNC and natural graphite



results of crystallinity via Raman spectroscopy and XRD. Because the development of the graphite structure of Ht-MNC was confirmed via XRD, the exposure of the edge plane is considered to be the cause of a lower I_G/I_D value than that of natural graphite. Conversely, Ht-MNC had a more graphitic structure than MNC and more edge planes than natural graphite, therefore, it might be highly reactive with Ca^{2+} . The interlayer distance also narrowed in the order of increasing graphitization degree. The BET analysis revealed that MNC has larger specific surface area and mesopores than natural graphite. However, Ht-MNC had smaller specific surface area and mesopores than MNC because of the large mean filament diameter.

FTIR spectroscopy was conducted to evaluate the solvation structure in GBL-based electrolytes containing $\text{Ca}(\text{ClO}_4)_2$ and $\text{Ca}(\text{TFSI})_2$, (Fig. 6). As shown in Fig. 6, the GBL solvent exhibited the peak of C=O double bond at 1750 cm^{-1} . For the electrolyte containing $\text{Ca}(\text{ClO}_4)_2$, a peak due to the perchlorate ion (ClO_4^-) at 1100 cm^{-1} was observed. For the electrolyte containing $\text{Ca}(\text{TFSI})_2$, peaks due to the TFSI⁻ anion appeared at 1060, 1141, 1228, and 1335 cm^{-1} corresponding to the S–O stretching vibrations, SO_2 symmetric stretching vibrations, CF_3 stretching vibrations, and SO_2 asymmetric stretching vibrations, respectively. In FTIR spectroscopy, when an interaction occurs with a material, the peak of the IR spectrum shifts or a new peak appears [35]. Each Ca salt was dissolved in the GBL solvent, but the C=O double bond peak did not change considerably. However, a new peak appeared at 1354 cm^{-1} for electrolytes containing $\text{Ca}(\text{TFSI})_2$; this peak could be derived from Ca-GBL.

Similarly, Raman spectroscopy was conducted to evaluate the strength of interaction between the solvent and each Ca salt (see Fig. 7). The GBL solvent exhibited the peak of C–O single bond at 930 cm^{-1} (Fig. 7a). Even when each Ca salt was dissolved, no new bands were observed, and the bandwidth displayed only approximately 2 cm^{-1} spreading. When each Ca salt was dissolved in EC- and PC-based electrolytes, new bands, derived from the solvated ions in which the solvent was coordinated to Ca^{2+} , appeared, and the width of the

bandshift was approximately in the range of $10\text{--}15\text{ cm}^{-1}$ [15]. Because the width of this bandshift represents the strength of interaction between the ion and solvent molecules [36], this result indicates that the interaction between Ca^{2+} and the GBL solvent was very weak. This agrees with the order of the dielectric constants of these solvents [EC: 89.8, PC: 64.9, and GBL: 39.1], the higher the dielectric constant, the more readily the solvation proceeded. For the electrolyte containing $\text{Ca}(\text{TFSI})_2$, however, a new peak appeared at 693 cm^{-1} . In Fig. 7b, such a peak cannot be confirmed even though the salt concentration increases; however, in Fig. 7c, the peak intensity increases as the concentration increases. Accordingly, for the electrolyte containing $0.5\text{ M Ca}(\text{TFSI})_2$, the peak at 693 cm^{-1} is attributed to the solvated ions i.e., Ca-GBL [37]. Therefore, $\text{Ca}(\text{TFSI})_2$ is highly likely to interact with the solvent; thus, the order of the strength of interaction with Ca^{2+} is $\text{Ca}(\text{ClO}_4)_2 < \text{Ca}(\text{TFSI})_2$.

Before testing the electrochemical performances of the anode materials, the AC quasi-reference electrode (AC QRE) was calibrated using a cyclic voltammogram of 0.05 M F_c in a GBL-based electrolyte containing $0.5\text{ M Ca}(\text{ClO}_4)_2$ and $0.5\text{ M Ca}(\text{TFSI})_2$, respectively, using a three-electrode cell. The Ca metal on the counter/reference electrodes for testing battery materials can only be used under limited conditions owing to irreversible plating/stripping due to the formation of a passivation layer. Thus, the use of the AC QRE, which facilitates stable evaluation in the potential window of the electrolyte, was proposed [1, 38, 39]. For non-aqueous systems, calibrating the AC QRE by measuring the redox potential of F_c as an internal standard is recommended. Accordingly, the reference potential of F_c/F_c^+ for the AC QRE was calculated as follows:

$$E_{\text{F}_c/\text{F}_c^+} = E_{1/2} = \frac{E_{\text{p,a}} + E_{\text{p,c}}}{2} \quad (2)$$

where $E_{\text{F}_c/\text{F}_c^+}$ denotes the redox potential of F_c , and can be obtained from the half-wave potential ($E_{1/2}$). $E_{\text{p,a}}$ and $E_{\text{p,c}}$ denote the anodic and cathodic peak potentials, respectively. Moreover, because $E_{\text{p,a}}$ was 0.130 V and $E_{\text{p,c}}$

Fig. 6 Fourier transform infrared (FTIR) spectrum for each electrolyte

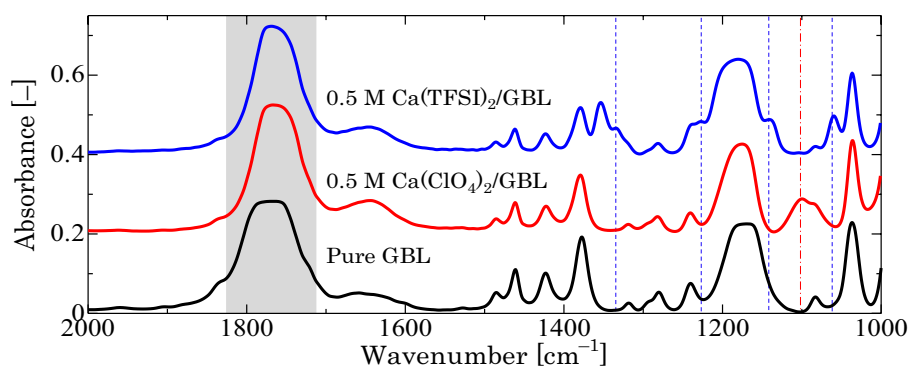
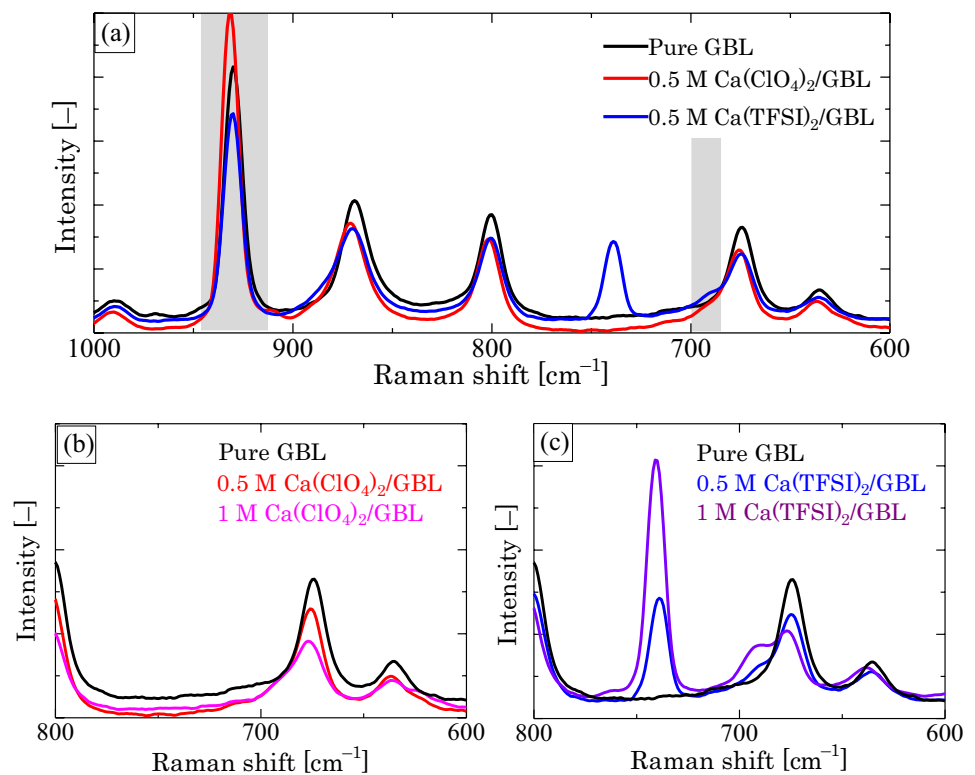


Fig. 7 Raman spectrum for **a** each electrolyte and pure γ -butyrolactone (GBL) solvent, **b** electrolytes containing Ca (ClO_4)₂, and **c** electrolytes containing Ca (TFSI)₂ at different concentrations



was -0.085 V , $E_{\text{Fc}/\text{Fc}^+}$ was 0.023 V versus AC QRE. Similarly, because $E_{\text{p,a}}$ was 0.090 V and $E_{\text{p,c}}$ was 0.020 V , $E_{\text{Fc}/\text{Fc}^+}$ was 0.055 V versus AC QRE. Therefore, the $E_{\text{Fc}/\text{Fc}^+}$ for the AC QRE obtained for each electrolyte is -0.377 V and -0.345 V lower than the $E_{\text{Fc}/\text{Fc}^+}$ for SHE. From this result, the potentials of Ca^{2+}/Ca versus AC QRE were calculated to be -3.247 and -3.215 V . Hereinafter, all the electrochemical potentials will describe the potential of AC QRE and calibrated potential of Ca^{2+}/Ca [20].

Figure 8 shows the charge/discharge curves of the MNC, Ht-MNC, and graphite electrodes in each electrolyte. In this study, charging is defined as reduction and Ca^{2+} or solvated Ca^{2+} intercalation, and discharging is defined as oxidation and Ca^{2+} deintercalation [25, 40, 41]. At present, it is not clear whether intercalation of Ca^{2+} or solvated Ca^{2+} into the graphite layer.

The electrolyte containing Ca (ClO_4)₂ showed higher charge/discharge capacity than the electrolyte containing Ca (TFSI)₂. Moreover, the charge/discharge capacity of the electrolyte containing Ca (ClO_4)₂ increased as the cycle progressed. Hence, we hypothesize that Ca^{2+} or solvated Ca^{2+} intercalation/deintercalation occurs more in the electrolyte containing Ca (ClO_4)₂. Next, MNC and Ht-MNC showed higher charge/discharge capacities than natural graphite in the case of the electrolyte containing Ca (ClO_4)₂. Natural graphite is spheroidized to suppress the excessive reductive decomposition of the electrolytes, whereas MNC is highly reactive with the electrolytes

owing to the exposed edge planes of the CNFs. However, Ht-MNC exhibited lower charge/discharge capacity than MNC. The charge/discharge capacity of MNC includes the capacity due to the amount of adsorption caused by the specific surface area. Consequently, the charge/discharge capacity of MNC is larger than Ht-MNC. In other words, Ht-MNC's Ca^{2+} or solvated Ca^{2+} intercalation proceeded more than in MNC. Therefore, we consider that compared with MNC, Ht-MNC has a higher ratio of intercalation capacity to total capacity. Additionally, the Coulombic efficiency was correlated with the degree of graphitization of each material. Conversely, for the electrolyte containing Ca (TFSI)₂, there was no considerable difference in charge/discharge capacity among the anode materials. This may be because Ca (TFSI)₂ strongly interacts with the solvent molecule, thereby making Ca^{2+} or solvated Ca^{2+} intercalation unlikely to occur.

XRD was conducted to evaluate the intercalation of Ca^{2+} or solvated Ca^{2+} between the graphene layers of each anode material (Fig. 9). Before charging, MNC and Ht-MNC had peaks at 25.81° and 26.30° corresponding to the (002) plane (Fig. 5a); for the electrolytes containing Ca (ClO_4)₂, the (002) peaks of MNC and Ht-MNC shifted to 19.94° and 19.91° , respectively, after charging and the interlayer distances increased to 0.445 nm and 0.446 nm , respectively. This indicates that Ca^{2+} or solvated Ca^{2+} intercalates between graphene layers. Furthermore, for Ht-MNCs, the shifted peaks slightly reverted after discharge. This is thought to be due

Fig. 8 Charge/discharge curves of the **a, b** natural graphite electrode, **c, d** Marimo nano carbon (MNC) electrode and **e, f** heat-treated MNC (Ht-MNC) electrode in **a, c, e** 0.5 M $\text{Ca}(\text{ClO}_4)_2/\gamma$ -butyrolactone (GBL) and **b, d, f** 0.5 M $\text{Ca}(\text{TFSI})_2/\text{GBL}$

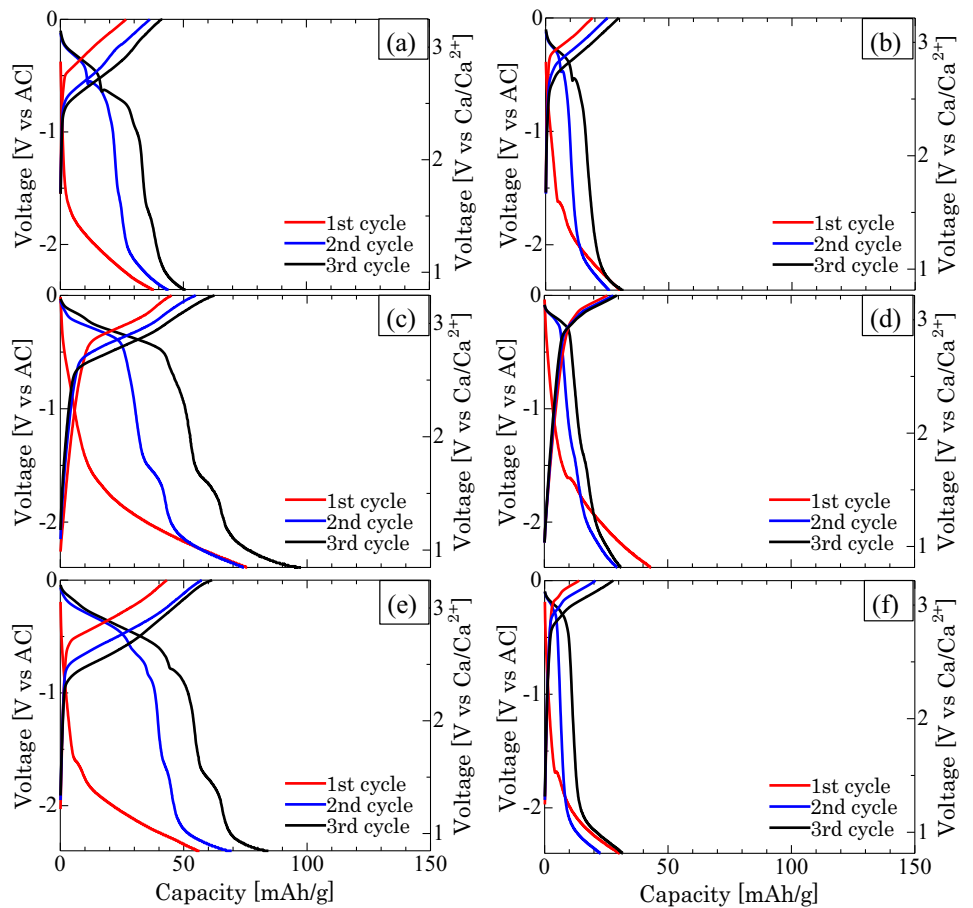
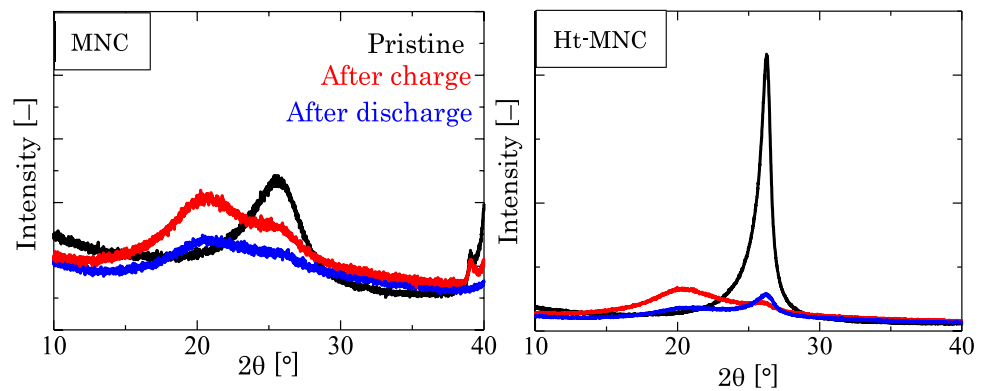


Fig. 9 X-ray diffractometry (XRD) spectra of Marimo nano carbon (MNC) and heat-treated MNC (Ht-MNC) before charge and after charging in 0.5 M $\text{Ca}(\text{ClO}_4)_2/\text{GBL}$



to development of the graphite structure, which facilitates reversible charging and discharging of Ca^{2+} or solvated Ca^{2+} . However, the shifted peak of MNC did not return to the original 2θ value at all, indicating that it cannot be successfully

discharged. This result is consistent with the Coulomb efficiency calculated from Fig. 8.

4 Conclusion

When MNCs were heat treated, their crystallinity was enhanced and graphite structure appeared. Moreover, when $\text{Ca}(\text{ClO}_4)_2$ and $\text{Ca}(\text{TFSI})_2$ were used as salts, the solution structure changed in GBL-based electrolytes, and the interaction strength with Ca^{2+} was in the order $\text{Ca}(\text{ClO}_4)_2 < \text{Ca}(\text{TFSI})_2$. For electrolytes containing $\text{Ca}(\text{ClO}_4)_2$ and $\text{Ca}(\text{TFSI})_2$, MNC and Ht-MNC were confirmed to exhibit higher charge/discharge capacity and reversible redox reactivity than natural graphite. Furthermore, Ht-MNC exhibited more advanced reversible Ca^{2+} or solvated Ca^{2+} intercalation between graphene layers than MNC.

Acknowledgements This work was supported by JSPS KAKENHI Grant Number JP20K12274. The authors are grateful to Nippon Graphite Industries, Ltd., for supplying them with spherical natural graphite for this research. The authors would like to thank Enago (www.enago.jp) for English language review.

Funding Funding was provided by Japan Society for the Promotion of Science (KAKENHI JP20K12274).

Declarations

Competing interests The authors declare that they have no known competing financial interests or personal relationships that could have appeared to influence the work reported in this paper.

Open Access This article is licensed under a Creative Commons Attribution 4.0 International License, which permits use, sharing, adaptation, distribution and reproduction in any medium or format, as long as you give appropriate credit to the original author(s) and the source, provide a link to the Creative Commons licence, and indicate if changes were made. The images or other third party material in this article are included in the article's Creative Commons licence, unless indicated otherwise in a credit line to the material. If material is not included in the article's Creative Commons licence and your intended use is not permitted by statutory regulation or exceeds the permitted use, you will need to obtain permission directly from the copyright holder. To view a copy of this licence, visit <http://creativecommons.org/licenses/by/4.0/>.

References

1. Dugas R, Forero-Saboya JD, Ponrouch A (2019) Methods and protocols for reliable electrochemical testing in post-Li batteries (Na, K, Mg, and Ca). *Chem Mater* 31:8613–8628
2. Liu Q, Wang H, Jiang C, Tang Y (2019) Multi-ion strategies towards emerging rechargeable batteries with high performance. *Energy Storage Mater* 23:566–586
3. Ponrouch A, Bitenc J, Dominko R, Lindahl N, Johansson P, Palacin MR (2019) Multivalent rechargeable batteries. *Energy Storage Mater* 20:253–262
4. Lipson AL, Pan B, Lapidua SH, Liao C, Vaughey J, Ingram BJ (2015) Rechargeable Ca-ion batteries: a new energy storage system. *Chem Mater* 27:8442–8447
5. Tojo T, Sugiura Y, Inada R, Sakurai Y (2016) Reversible calcium ion batteries using a dehydrated Prussian Blue analogue cathode. *Electrochim Acta* 207:22–27
6. Siegal MP, Yelton WG, Perdue BR, Sava Gallis DF, Schwarz H (2016) Nanoporous-carbon as a potential host material for reversible Mg ion intercalation. *J Electrochem Soc* 163:A1030–A1035
7. Deivanayagam R, Ingram BJ, Shahbazian-Yassar R (2019) Progress in development of electrolytes for magnesium batteries. *Energy Storage Mater* 21:136–153
8. Arroyo-de Dompablo ME, Ponrouch A, Johansson P, Palacin M (2020) Achievements, challenges, and prospects of calcium batteries. *Chem Rev* 120:6331–6357
9. Gummow RJ, Vamvounis G, Kannan MB, He Y (2018) Calcium-ion batteries: current state-of-the-art and future perspectives. *Adv Mater* 30:e1801702
10. Stievano L, Meazza I, Bitenc J, Cavallo C, Brutti S, Navarra MA (2021) Emerging calcium batteries. *J Power Sources* 482:228875
11. Alekseenko V, Alekseenko A (2014) The abundances of chemical elements in urban soils. *J Geochem Explor* 147:245–249
12. Park J, Xu ZL, Yoon G, Park SK, Wang J, Hyun H, Park H, Lim J, Ko YJ, Yun YS, Kang K (2020) Stable and high-power calcium-ion batteries enabled by calcium intercalation into graphite. *Adv Mater* 32:1904411
13. Aurbach D, Skaletsky R, Gofer Y (1991) The electrochemical behavior of calcium electrodes in a few organic electrolytes. *J Electrochem Soc* 138:3536–3545
14. Ponrouch A, Frontera C, Bardé F, Palacin M (2016) Towards a calcium-based rechargeable battery. *Nat Mater* 15:169–172
15. Forero-Saboya JD, Marchante E, Araujo RB, Monti D, Johansson P, Ponrouch A (2019) Cation solvation and physico-chemical properties of Ca battery electrolytes. *J Phys Chem C* 123:29524–29532
16. Cabello M, Nacimiento F, González JR, Ortiz G, Alcántara R, Lavela P, Pérez-Vicente C, Tirado JL (2016) Advancing towards a veritable calcium-ion battery: CaCo_2O_4 positive electrode material. *Electrochem Commun* 67:59–64
17. Amatucci GG, Badway F, Singhal A, Beaudoin B, Skandan G, Bowmer T, Plitz I, Pereira N, Chapman T, Jaworski R (2001) Investigation of yttrium and polyvalent ion intercalation into nanocrystalline vanadium oxide. *J Electrochem Soc* 148:A940–A950
18. Hayashi M, Arai H, Ohtsuka H, Sakurai Y (2003) Electrochemical characteristics of calcium in organic electrolyte solutions and vanadium oxides as calcium hosts. *J Power Sources* 119–121:617–620
19. Kuperman N, Padigi P, Goncher G, Evans D, Thiebes J, Solanki R (2017) High performance Prussian Blue cathode for nonaqueous Ca-ion intercalation battery. *J Power Sources* 342:414–418
20. Lipson AL, Han SD, Kim S, Pan B, Sa N, Liao C, Fister TT, Burrell AK, Vaughey JT, Ingram BJ (2016) Nickel hexacyanoferrate, a versatile intercalation host for divalent ions from nonaqueous electrolytes. *J Power Sources* 325:646–652
21. Ogumi Z, Inaba M (1998) Electrochemical lithium intercalation within carbonaceous materials: intercalation process, surface film formation, and lithium diffusion. *Bull Chem Soc* 71:521–534
22. Herold C, Emery N, Maréché JF, Lagrange P (2008) Synthesis and superconducting properties of bulk CaC_6 GIC. *TANSO* 233:166–173
23. Sugawara K, Sato T, Takahashi T (2009) Fermi-surface-dependent superconducting gap in C_6Ca . *Nat Phys* 5:40–43
24. Yang SL, Sobota JA, Howard CA, Pickard CJ, Hashimoto M, Lu DH, Mo SK, Kirchmann PS, Shen ZX (2014) Superconducting graphene sheets in CaC_6 enabled by phonon-mediated interband interactions. *Nat Commun* 5:3493
25. Richard Prabakar SJ, Ikhe AB, Park WB, Chung KC, Park H, Kim KJ, Ahn D, Kwak JS, Sohn KS, Pyo M (2019) Graphite as a long-life

- Ca²⁺-intercalation anode and its implementation for rocking-chair type calcium-ion batteries. *Adv Sci* 6:1902129
26. Nakagawa K, Oda H, Yamashita A, Okamoto M, Sato Y, Gamo H, Gamo MN, Ogawa K, Ando T (2009) A novel spherical carbon. *J Mater Sci* 44:221–226
 27. Saifuddin N, Raziah AZ, Junizah AR (2012) Carbon nanotubes: a review on structure and their interaction with proteins. *J Chem* 2013:18
 28. Muraoka K, Tsujino G, Nakagawa K, Oda H, Ando T (2016) Electrochemical properties of various carbon nanofilaments for use as Li-ion battery anodes. *Trans Mater Res Soc Jpn* 41:81–84
 29. Nakagawa K, Yamagishi M, Nishimoto H, Ikenaga N, Kobayashi T, Gamo MN, Suzuki T, Ando T (2003) Oxidized diamond as a simultaneous production medium of carbon nanomaterials and hydrogen for fuel cell. *Chem Mater* 15:4571–4575
 30. Eguchi M, Okubo A, Yamamoto S, Kikuchi M, Uno K, Kobayashi Y, Gamo MN, Ando T (2010) Preparation of catalyst for a polymer electrolyte fuel cell using a novel spherical carbon support. *J Power Sources* 195:5862–5867
 31. Tsujino G, Ota H, Gamo MN, Nakagawa K, Oda H (2015) Synthesis of various nano carbon filaments by CVD over catalysts loaded on a metal oxides composite. *TANSO* 2015:2–6
 32. Nishimura Y, Nakatani N, Nakagawa K (2021) Role of solution structure in the electrochemical intercalation of Ca²⁺ into graphite layers. *J Solid State Electrochem* 25:2495–2501
 33. Yan X, Wei J, Guo J, Hua C, Liu J, Chen L, Hei L, Li C (2017) Mechanism of graphitization and optical degradation of CVD diamond films by rapid heating treatment. *Diam Ralat Mater* 73:39–46
 34. Maheshwari PH, Singh R, Mathur RB (2012) Effect of heat treatment on the structure and stability of multiwalled carbon nanotubes produced by catalytic chemical vapor deposition technique. *Mater Chem Phys* 134:412–416
 35. Ha SY, Lee YW, Woo SW, Koo B, Kim JS, Cho J, Lee KT, Choi NS (2014) Magnesium(II) bis(trifluoromethane sulfonyl) imide-based electrolytes with wide electrochemical windows for rechargeable magnesium batteries. *ACS Appl Mater Interfaces* 6:4063–4073
 36. Yamaguchi T, Kimura Y, Hirota N (1998) Solvation state selective excitation in resonance Raman spectroscopy. II. Theoretical calculation. *J Chem Phys* 109:9084
 37. Forero-Saboya JD, Marchante E, Araujo RB, Monti D, Johansson P, Ponrouch A (2019) Cation solvation and physicochemical properties of Ca battery electrolytes. *J Phys Chem* 123:29524–29532
 38. Liu X, Elia GA, Passerini S (2020) Evaluation of counter and reference electrodes for the investigation of Ca battery materials. *J Power Sources Adv* 2:100008
 39. Ruch PW, Cericola D, Hahn M, Kötz R, Wokaun A (2009) On the use of activated carbon as a quasi-reference electrode in non-aqueous electrolyte solutions. *J Electroanal Chem* 636:128–131
 40. God C, Bitschnau B, Kapper K, Lenardt C, Schmuck M, Mautner F, Koller S (2017) Intercalation behavior of magnesium into natural graphite using organic electrolyte systems. *RSC Adv* 7:14168–14175
 41. Takeuchi S, Fukutsuka T, Miyazaki K, Abe T (2018) Lithium-ion intercalation by calcium-ion addition in propylene carbonate-trimethyl phosphate electrolyte solution. *J Electrochem Soc* 165:A349–A354

Publisher's Note Springer Nature remains neutral with regard to jurisdictional claims in published maps and institutional affiliations.